Journal of Nuclear Materials 395 (2009) 120–130

Contents lists available at ScienceDirect

Journal of Nuclear Materials

journal homepage: www.elsevier.com/locate/jnucmat

Effect of dislocations on spinodal decomposition in Fe–Cr alloys

Yong-Sheng Li [a,b], Shu-Xiao Li [b,c], Tong-Yi Zhang [a,b,*]

[a] Department of Mechanical Engineering, Hong Kong University of Science and Technology, Clear Water Bay, Kowloon, Hong Kong, China
[b] The Hong Kong-Beijing UST Joint Research Center, HKUST, Fok Ying Tung Graduate School, Nansha, Guangzhou 511458, China
[c] State Key Laboratory of Advance Metals and Materials, University of Science and Technology Beijing, Xueyuan Road, Beijing 100083, China

ARTICLE INFO

Article history:
Received 7 June 2009
Accepted 2 October 2009

ABSTRACT

Phase-field simulations of spinodal decomposition in Fe–Cr alloys with dislocations were performed by using the Cahn–Hilliard diffusion equation. The stress field of dislocations was calculated in real space via Stroh's formalism, while the composition inhomogeneity-induced stress field and the diffusion equation were numerically calculated in Fourier space. The simulation results indicate that dislocation stress field facilitates, energetically and kinetically, spinodal decomposition, making the phase separation faster and the separated phase particles bigger at and near the dislocation core regions. A tilt grain boundary is thus a favorable place for spinodal decomposition, resulting in a special microstructure morphology, especially at the early stage of decomposition.

1. Introduction

Grain boundaries and dislocations are thermodynamically favorable sites for precipitates. The profile of grain boundaries or a dislocation network may control the morphology and distribution of precipitates. Theoretical analysis based on thermodynamics has been carried out to study the energy change before and after precipitation. For example, Cahn [1] theoretically calculated the activation energy to form an incoherent precipitate on a dislocation. His results show that the nucleation energy decreases even more rapidly with increasing thermodynamic driving force, than does the nucleation energy for homogeneous nucleation, becoming zero at a finite value of the supersaturation. Dollins [2] analyzed the free energy change induced by a coherent precipitate on a dislocation. Assuming that the strain field of the dislocation was unaltered by the precipitate, he calculated the interaction energy with the consideration of the precipitate shape and the elastic misfit between the precipitate and the matrix [2]. In addition to the thermodynamic analysis, the kinetics of stress-assisted precipitation on dislocations has also been investigated [3–5] because the morphology and distribution of precipitates may be finally determined by the kinetic process. Cottrell and Bilby [3] gave an approximate calculation of the stress-assisted precipitation on dislocations by neglecting the diffusion flux induced by concentration gradient. Therefore, their result is more accurate at the very early stages of precipitation. Ham [4] developed a kinetic theory for the rate of stress-assisted precipitation on dislocations by including both concentration gradient- and stress gradient-induced diffusion fluxes. He first calculated the time-dependent rate of precipitation on an isolated dislocation and then used the results to calculate the short-time part of the precipitation curve for an array of dislocations, while the long-time part of the precipitation curve was established by using steady-state solutions to the diffusion equation with a variational procedure. Clearly, thermodynamic analysis and kinetic calculations must be combined together and solved simultaneously to predict the morphology and distribution of precipitates, which leads to the development of phase-field simulations.

Phase-field simulations are based on fundamental principles of thermodynamics and kinetics and thus are powerful in prediction of the temporal evolution of microstructures in materials [6–10]. In a phase-field model, thermodynamic energies are described in terms of a set of continuous order parameters. The temporal evolution of a microstructure is obtained by solving kinetics equations that govern the time-dependence of the spatially inhomogeneous order parameters. Phase-field simulations do not make any prior assumptions about transient microstructures, which may appear during a phase transformation path, and about transformation criteria. Phase transformation is a direct consequence of the minimization process of the total free energy of an entire simulated system.

Phase-field simulations of spinodal decomposition are based on the Cahn–Hilliard diffusion equation [11,12], in which thermodynamic energies are described in terms of the solute concentration. Recently, phase-field simulations have been conducted to study spinodal decomposition in alloys with dislocations [13–15] and to investigate dislocation formation and dislocation dynamics [16–19]. For instance, Léonard and Desai [13] conducted phase-field simulations of spinodal decomposition in an isotropic alloy

* Corresponding author. Address: Department of Mechanical Engineering, Hong Kong University of Science and Technology, Clear Water Bay, Kowloon, Hong Kong, China. Tel.: +852 2358 7192; fax: +852 2358 1543.
E-mail address: mezhangt@ust.hk (T.-Y. Zhang).

0022-3115/$ - see front matter © 2009 Elsevier B.V. All rights reserved.
doi:10.1016/j.jnucmat.2009.10.042

with dislocations. They derived the stress field of dislocations in an infinite medium in real space and conducted the simulations with periodic boundary conditions in Fourier space. Applying Fourier transformation with the periodic boundary conditions implies that a simulated system is a representative cell in a two- or three-dimensional periodic array of cells. Thus, the stress field of dislocations in the representative cell should be calculated from dislocations in all cells of the periodic array. Only when the representative cell was sufficiently large, the effect of periodic boundary conditions on the stress field of the dislocations might be approximately ignored. Their results illustrate that the decomposition process was accelerated when the dislocation density increased [13]. Hu and Chen [20] investigated coherent precipitation around an edge dislocation in an anisotropic medium. The stress field of a dislocation was solved in Fourier space with the periodic boundary conditions by using Mura's [21] dislocation eigenstrain method. They found that a direct use of the dislocation eigenstrain method resulted in a significant oscillation in the stress field. This is because Mura's [21] dislocation eigenstrain method is valid for an infinite domain, rather than for a finite representative cell. They proposed two approaches to get rid of the oscillation. The first one is to calculate a dislocation loop and the other is to use a Gaussian function to describe the Burgers vector distribution. Their results show that coherent nucleation of a new phase may become barrierless due to the dislocation stress field [20]. Ni and He [14] and Hu and Chen [15], by using the dislocation eigenstrain method [21], investigated the composition pattern of spinodal decomposition in thin films with subsurfacial and interfacial dislocation arrays, respectively [14,15]. Their results show that the periodic stress field associated with the dislocation array leads to a directional phase separation and the formation of ordered mesoscale microstructures. When the dislocation periodicity is small, the wavelength of the ordered microstructure tends to have the same periodicity as the dislocation array.

The present study simulates the phase separation process of Fe–Cr alloys with dislocations by using the thermodynamic function of the alloys. Fe–Cr alloys have found wide applications in nuclear power plants [22–24] due to their higher swelling resistance, high-corrosion resistance and good mechanical properties [25,26]. The mechanical properties of Fe–Cr alloys depend greatly on the morphology and profile of spinodal decomposition products of Fe-rich α phase and Cr-rich α' phase [27]. That is why intensity research has been carried out on spinodal decomposition in Fe–Cr alloys, especially on the morphology and profile of spinodal decomposition products. For example, Miller et al. [28] and Hyde et al. [29,30] conducted comprehensive experimental, theoretical and numerical investigations of spinodal decomposition in Fe–Cr alloys. They found a power law for the evolution of spinodal decomposition-induced microstructures and their experimental data illustrated fractal interfaces between Fe-rich α and Cr-rich α' regions. However, the interaction between dislocations and spinodal decomposition in Fe–Cr alloys has not been systematically studied yet. That motivates us to comprehensively investigate the role of dislocations in spinodal decomposition of Fe–Cr alloys by using phase-field simulations.

2. Phase-field model

In phase-field simulations, the concentration of an alloy is usually taken as the order parameter. The temporal evolution of the concentration is described by the Cahn–Hilliard diffusion equation [11,12],

$$\frac{\partial c(\mathbf{x},t)}{\partial t} = \nabla\cdot\left[M\cdot\nabla\left(\frac{\delta F}{\delta c}\right)\right] \tag{1}$$

where M denotes the mobility, c is the atom fraction of Cr element, F is the total free energy of the simulated system, and $\mathbf{x} = (x_1, x_2, x_3)$ and t denote the spatial coordinates and time, respectively. The total free energy is given by

$$F = \int_V \left[f(c) + \frac{1}{2}\alpha(\nabla c)^2 + E_{el}\right]dV, \tag{2}$$

where $f(c)$ is the local chemical free energy density per unit volume, the second term represents the concentration gradient energy per unit volume, and E_{el} is the elastic energy density per unit volume. Based on the regular solution approximation, the chemical free energy density per unit volume of a Fe–Cr alloy is given by

$$f(c) = \frac{1}{V_m}\Big\{(1-c)G^0_{Fe} + cG^0_{Cr} + \Omega_{FeCr}c(1-c) + RT[c\ln c + (1-c)\ln(1-c)]\Big\}, \tag{3}$$

where G^0_{Fe} and G^0_{Cr} are the standard molar Gibbs free energy of pure Fe and Cr, respectively, Ω_{FeCr} is the interaction parameter, R is gas constant, T is the absolute temperature, and V_m denotes the molar volume of the alloy. $G^0_{Fe} = G^0_{Cr} = 0$ was adopted as the reference energy level for the Gibbs free energy, $\Omega_{FeCr} = 20500 - 9.68T$ [31]. The first-order differential of $f(c)$ to composition can give the Fe–Cr phase diagram, as shown in Fig. 1. The concentration gradient coefficient is expressed by [32,33]

$$\alpha = \frac{1}{V_m}\frac{1}{6}r_0^2\Omega_{FeCr}, \tag{4}$$

where r_0 is the interatomic distance at stress-free state and changes with composition by simply obeying Vergard's law. In the present work, we assume the mobility to be a constant for simplicity. Then, substituting Eq. (2) into Eq. (1) yields

$$\frac{\partial c(\mathbf{x},t)}{\partial t} = M\nabla^2\left[\frac{\delta f(c)}{\delta c} - \alpha\nabla^2 c + \frac{\delta E_{el}}{\delta c}\right]. \tag{5}$$

Eq. (5) is the fundamental equation to be solved in the phase-field simulations.

2.1. Stress field induced by composition inhomogeneity

Elastic strain ε^{in}_{ij} induced by the composition inhomogeneity is the difference between total strain ε_{ij} and eigenstrain ε^0_{ij} [34]:

$$\varepsilon^{in}_{ij} = \varepsilon_{ij} - \varepsilon^0_{ij}. \tag{6}$$

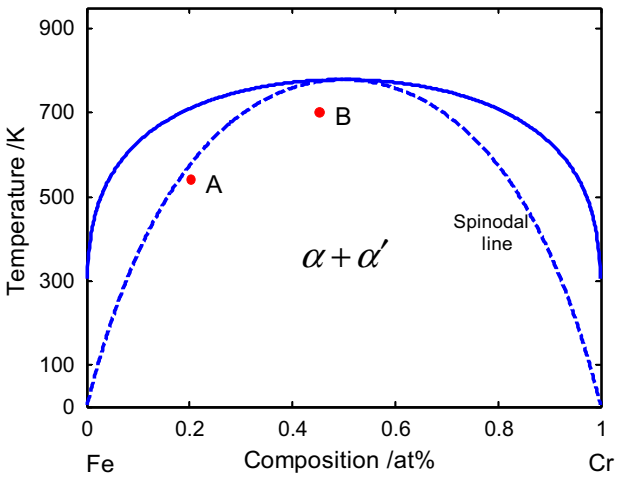

Fig. 1. The miscibility gap of Fe–Cr alloy phase diagram and the two simulated alloys. The solid line represents the phase separation curve and the dotted line is the spinodal decomposition curve.

Table 1
Elastic constants of Fe and Cr (10^{11} Pa) [38].

	Fe	Cr
C_{11}	2.3310	3.5000
C_{12}	1.3544	0.6780
C_{44}	1.7830	1.0080

The eigenstrain is given by $\varepsilon^0_{ij} = \varepsilon_0 \delta_{ij} \delta c$, in which $\varepsilon_0 = (1/a)\,(da/dc)$ is the composition expansion coefficient of lattice parameter. $\delta c = c - c_0$ with c_0 being the nominal composition of the alloy, and δ_{ij} is the Kronecker-delta function. The total strain is related to displacements u_i by the kinematic equation:

$$\varepsilon_{kl} = \frac{1}{2}\left\{\frac{\partial u_k}{\partial x_l} + \frac{\partial u_l}{\partial x_k}\right\}. \tag{7}$$

Hook's law links elastic stress tensor to elastic strain tensor as

$$\sigma^{in}_{ij} = C_{ijkl}\varepsilon^{in}_{kl} = (\varepsilon_{kl} - \varepsilon^0_{kl}) \tag{8}$$

with elastic constant tensor C_{ijkl}. For a given distribution of composition, the system should always satisfy mechanical equilibrium, which requires

$$\frac{\partial \sigma^{in}_{ij}}{\partial x_j} = 0 \tag{9}$$

for a body-force-free system, because elastic response is much faster than the diffusion process. If the elastic constants are assumed to be independent of composition, the mechanical equilibrium can be expressed by displacements and eigenstrains:

$$C_{ijkl}\frac{\partial^2 u_k}{\partial x_j \partial x_l} = C_{ijkl}\left[\varepsilon_0 \delta_{kl}\frac{\partial \delta c}{\partial x_j}\right]. \tag{10}$$

Solving Eq. (10) in Fourier space, we have

$$\tilde{u}_k(\mathbf{k}) = -iG_{ik}(\mathbf{k})\sigma^0_{ij}\delta\tilde{c}\,(\mathbf{k})\,k_j, \tag{11a}$$

where $\mathbf{k} = (k_1, k_2, k_3)$ is the reciprocal space wave vector, $i = \sqrt{-1}$, $G_{ik}(\mathbf{k})$ is the inverse tensor of $G^{-1}_{ik}(\mathbf{k}) = C_{ijkl}k_j k_l$, and $\sigma^0_{ij} = C_{ijkl}\varepsilon_0\delta_{kl}$. The total strain in Fourier space is then given by

$$\tilde{\varepsilon}_{ij}\,(\mathbf{k}) = \frac{i}{2}[\tilde{u}_i(\mathbf{k})k_j + \tilde{u}_j(\mathbf{k})k_i]. \tag{11b}$$

2.2. Stress field of dislocations

For two-dimensional linear anisotropic elasticity, Stroh's formalism [35] gives the general solutions,

$$\mathbf{u} = \mathbf{A}\mathbf{f}(z_\alpha) + \overline{\mathbf{A}\mathbf{f}(z_\alpha)}, \tag{12a}$$

$$\phi = \mathbf{B}\mathbf{f}(z_\alpha) + \overline{\mathbf{B}\mathbf{f}(z_\alpha)}, \tag{12b}$$

where $\mathbf{u}$ and ϕ are the displacement and stress function vectors, respectively, $\mathbf{A}$ and $\mathbf{B}$ are the eigenvector matrixes determined by the elastic constants and orientation of the alloy sample; $\mathbf{f}(z_\alpha) = [f_1(z_1), f_2(z_2), f_3(z_3)]^T$ is an analytic vector of $z_\alpha = x_1 + p_\alpha x_2 (\alpha = 1, 2, 3)$ to be determined by boundary conditions; and p_α with $\mathrm{Im}(p_\alpha) > 0$ is the eigenvalue of the eigen-equation

$$\mathbf{N}\xi = p\xi. \tag{13a}$$

In Eq. (13a),

$$\xi = \begin{pmatrix} A \\ B \end{pmatrix} \tag{13b}$$

is the eigenvector with A and B being the column vectors of $\mathbf{A}$ and $\mathbf{B}$, respectively; and the matrix $\mathbf{N}$ is given by

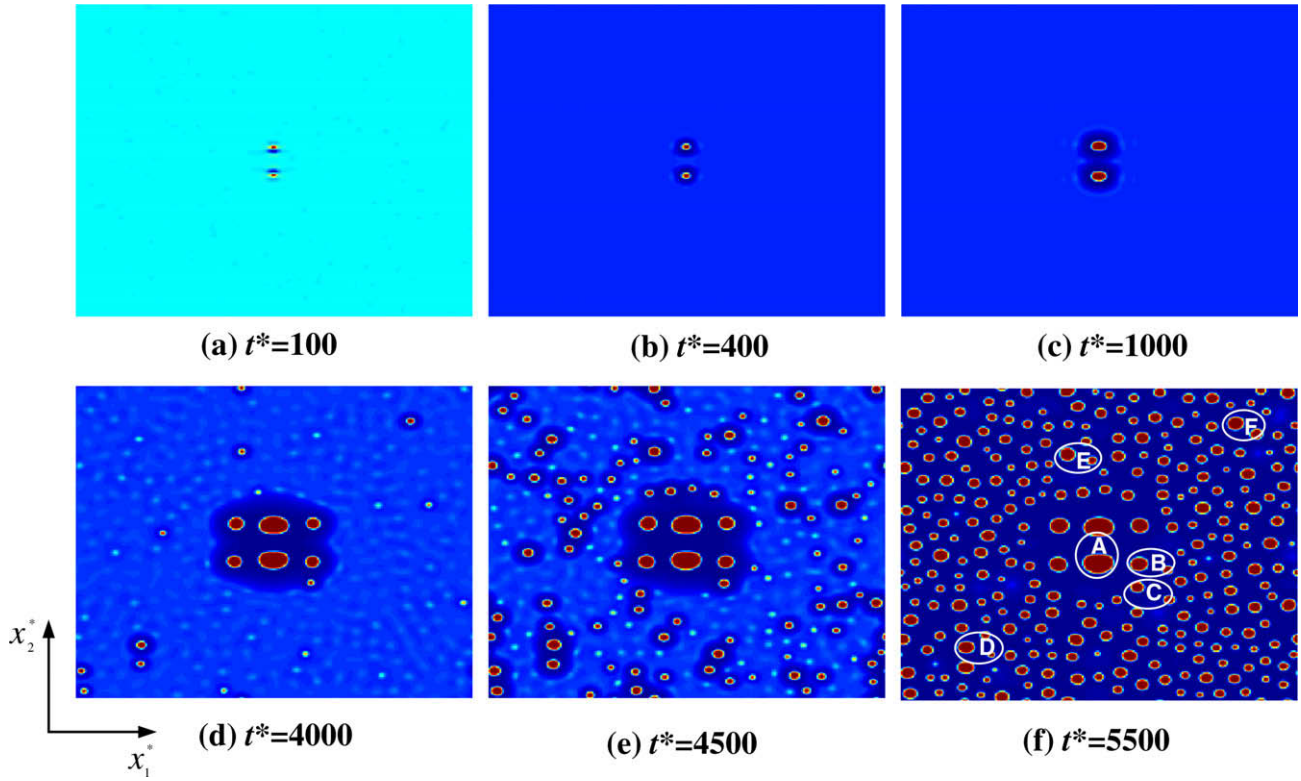

Fig. 2. Phase separation with two edge dislocations in the $c_0 = 0.2$ Fe–Cr alloy aged at 535 K.

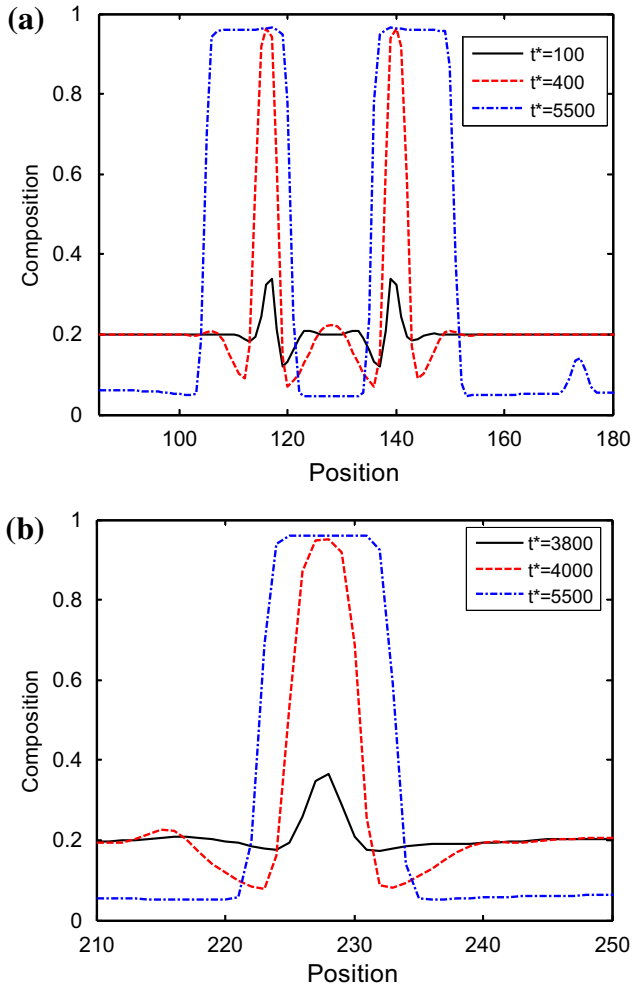

Fig. 3. Composition evolution (a) through the dislocation center along the x_2^* direction in Fig. 2 and (b) though the center of particle F along the x_2^* direction in Fig. 2f.

$$\mathbf{N} = \begin{pmatrix} \mathbf{N}_1 & \mathbf{N}_2 \\ \mathbf{N}_3 & \mathbf{N}_1^T \end{pmatrix}, \tag{13c}$$

with

$$\mathbf{N}_1 = -\mathbf{T}^{-1}\mathbf{R}^T, \quad \mathbf{N}_2 = \mathbf{T}^{-1} = \mathbf{N}_2^T, \quad \mathbf{N}_3 = \mathbf{R}\mathbf{T}^{-1}\mathbf{R}^T - \mathbf{Q} = \mathbf{N}_3^T, \tag{13d}$$

where

$$Q_{ik} = C_{i1k1}, \quad R_{ik} = C_{i1k2}, \quad T_{ik} = C_{i2k2}. \tag{13e}$$

Matrixes **A** and **B** have the following properties:

$$\mathbf{A}\mathbf{A}^T + \overline{\mathbf{A}\mathbf{A}^T} = \mathbf{B}\mathbf{B}^T + \overline{\mathbf{B}\mathbf{B}^T} = 0, \tag{14a}$$

$$\mathbf{B}\mathbf{A}^T + \overline{\mathbf{B}\mathbf{A}^T} = \mathbf{A}\mathbf{B}^T + \overline{\mathbf{A}\mathbf{B}^T} = \mathbf{I}, \tag{14b}$$

where **I** is the identity matrix. The stress field is calculated from the stress function vector as:

$$\sigma_{i2} = \phi_{i,1}, \quad \sigma_{i1} = -\phi_{i,2}. \tag{15}$$

For a line dislocation located at z_α^d in an infinite body, the two-dimensional solution is given with the analytic vector in the form of [36,37]

$$F(z_\alpha) = \langle \ln(z_\alpha - z_\alpha^d) \rangle \frac{1}{2\pi i}\mathbf{B}^T\mathbf{b}, \tag{16}$$

where the angle bracket denotes a diagonal matrix and $\mathbf{b} = (b_1, b_2, b_3)^T$ is the Burgers vector of the dislocation. Using

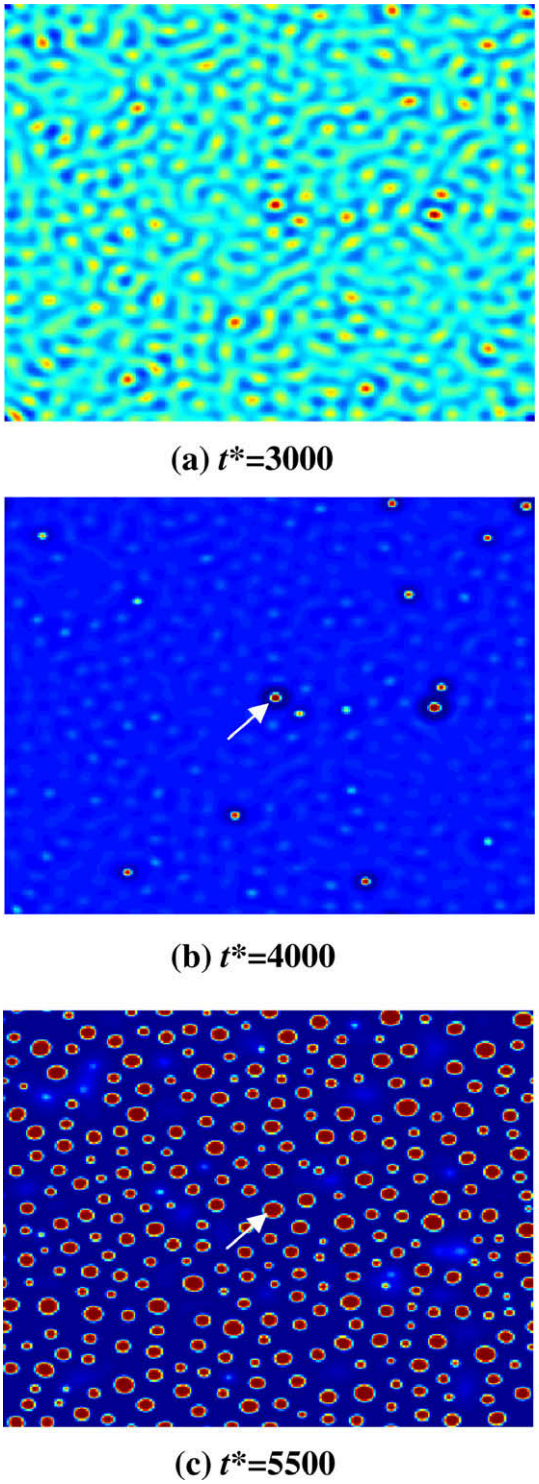

Fig. 4. Phase separation without any dislocations in the $c_0 = 0.2$ Fe–Cr alloy aged at 535 K.

superposition, we have the analytic vector for periodic dislocations with the same Burgers vector in an infinite space. If there is only a dislocation located at $x_{1,i}$ and $x_{2,i}$ in the representative cell, the analytic vector is given by

$$f_i = \left\langle \sum_{m=-\infty}^{\infty} \sum_{n=-\infty}^{\infty} \ln\{(x_1 + p_\alpha x_2) - [(mL_{x_1} + p_\alpha nL_{x_2}) + (x_{1,i} + p_\alpha x_{2,i})]\} \right\rangle \frac{1}{2\pi i}\mathbf{B}^T\mathbf{b}_i, \tag{17}$$

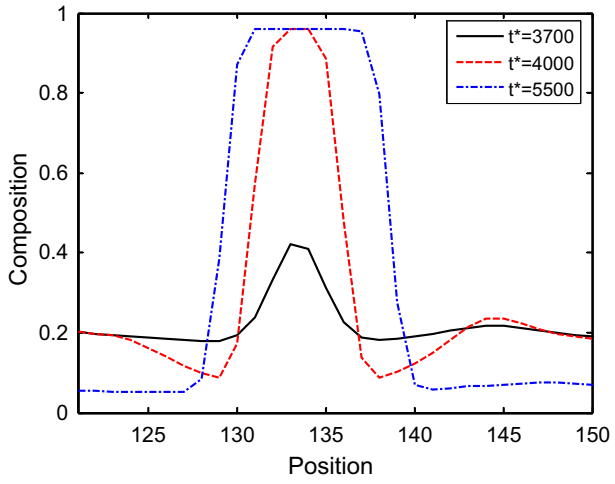

Fig. 5. Composition evolution through the particle labeled with an arrow in Figs. 4b and c along the x_2^* direction.

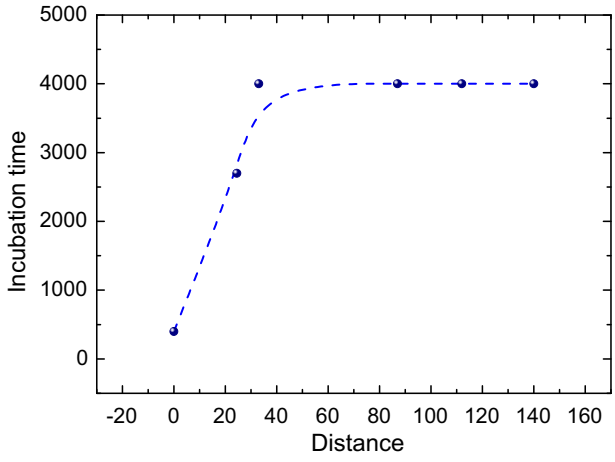

Fig. 6. The incubation time versus the distance from the dislocation core in the $c_0 = 0.2$ Fe–Cr alloy aged at 535 K.

where L_{x_1} and L_{x_2} are the dimensions of the representative cell in the x_1 and x_2 directions, respectively, and $\mathbf{b}_i$ is the Burgers vector of the dislocation. Using the basic sum formula $\sum_{n=-\infty}^{\infty} \frac{1}{n+a} = \pi \cot \pi a$, we reduce Eq. (17) to

$$f_i = \left\langle \sum_{m=-\infty}^{\infty} \ln \left\{ \sin \left[\pi \frac{(x_1 + p_\alpha x_2) - (x_{1,i} + p_\alpha x_{2,i}) - mL_{x_1}}{-p_\alpha L_{x_1}} \right] \right\} \right\rangle \times \frac{1}{2\pi i} \mathbf{B}^T \mathbf{b}_i. \tag{18a}$$

A small angle tilt grain boundary can be regarded as a dislocation wall with the relationship that $\theta = b/D$, where θ is the tilt angle, b is the Burger vector, and D is the dislocation spacing. For a dislocation wall parallel to the x_2 direction, Eq. (18a) is re-written as

$$f_i = \left\langle \sum_{m=-\infty}^{\infty} \ln \left\{ \sin \left[\pi \frac{(x_1 + p_\alpha x_2) - (x_{1,i} + p_\alpha x_{2,i}) - mL_{x_1}}{-p_\alpha D} \right] \right\} \right\rangle \times \frac{1}{2\pi i} \mathbf{B}^T \mathbf{b}_i. \tag{18b}$$

The analytic vector for n dislocations in the representative cell is thus given by

$$f = \sum_{i=1}^{n} f_i. \tag{19}$$

The dislocation stress can be obtained from Eq. (12a) by using the relation of displacement and strain.

$$\varepsilon_{kl}^d = \frac{1}{2} \left\{ \frac{\partial u_k^d}{\partial x_l} + \frac{\partial u_l^d}{\partial x_k} \right\}. \tag{20}$$

The total elastic strain of system includes the compositional inhomogeneity-induced strain ε_{ij}^{in} and the strain ε_{ij}^d induced by dislocations

$$\varepsilon_{ij}^t = \varepsilon_{ij}^{in} + \varepsilon_{ij}^d. \tag{21}$$

Then, the elastic strain energy density per unit volume is given by

$$E_{el} = \frac{1}{2} C_{ijkl} \varepsilon_{ij}^t \varepsilon_{kl}^t = \frac{1}{2} C_{ijkl} \left(\varepsilon_{ij} - \varepsilon_{ij}^0 + \varepsilon_{ij}^d \right) \left(\varepsilon_{kl} - \varepsilon_{kl}^0 + \varepsilon_{kl}^d \right). \tag{22}$$

2.3. Numerical calculations

In the present simulations, the edge dislocation was introduced on the $(1\bar{1}0)$ slip plane with Burger's vector $\mathbf{b} = a_0/2[111]$, where a_0 is the lattice constant of the Fe–Cr alloy with $c = 0.5$. The magnitude of Burger's vector was assumed to be a constant independent of composition and used as a length unit. The coordinates were constructed with axes x, y and z along the $[1\bar{1}0]$, $[111]$ and $[\bar{1}\bar{1}2]$ directions, respectively. We introduce the following dimensionless parameters,

$$\mathbf{x}^* = \mathbf{x}/|\mathbf{b}|, \quad t^* = tM\mu V_m/|\mathbf{b}^2|, \quad f^* = f/\mu, \quad \alpha^* = \alpha/(\mu|\mathbf{b}^2|), \quad E_{el}^* = E_{el}/\mu,$$

where μ is the shear modulus of Cr, $|\mathbf{b}|$ is the magnitude of Burgers vector $\mathbf{b} = a_0/2[111]$, the grid size is chosen as $\Delta x_1 = \Delta x_2 = |\mathbf{b}|$.

Using the dimensionless variables, Eq. (5) takes the form:

$$\frac{\partial c(\mathbf{x}^*, t^*)}{\partial t^*} = (\nabla^*)^2 \left[\frac{\delta f^*(c)}{\delta c} - \alpha^* (\nabla^*)^2 c + \frac{\delta E_{el}^*}{\delta c} \right]. \tag{23}$$

Fourier transformation of Eq. (23) yields

$$\frac{\partial c(\mathbf{k}^*, t^*)}{\partial t^*} = -(k^*)^2 \left[\left(\frac{\delta f^*(c)}{\delta c} + \frac{\delta E_{el}^*}{\delta c} \right)_{k^*} + \alpha^* (k^*)^2 c(\mathbf{k}^*) \right], \tag{24}$$

where k^* is the magnitude of $\mathbf{k}^*$, $c(\mathbf{k}^*)$ and $\left(\frac{\delta f^*(c)}{\delta c} + \frac{\delta E_{el}^*}{\delta c} \right)_{k^*}$ are the Fourier transformation of $c(r^*)$ and $\frac{\delta f^*(c)}{\delta c} + \frac{\delta E_{el}^*}{\delta c}$, respectively. Solving Eq. (24) numerically gives the temporal local composition in Fourier space and the results in real space are then obtained by inverse Fourier transformation. The simulation cell length is $L_{x_1} = N\Delta x_1$ and $L_{x_2} = M\Delta x_2$, where N and M and Δx_1 and Δx_2 are the grid numbers and grid size along the x_1 and x_2 directions, respectively. The dimensionless grid sizes are set to be $\Delta x_1^* = 1.0$ and $\Delta x_2^* = 1.0$ in the simulations. The lattice parameters are $a_{Fe} = 0.2866$ nm and $a_{Cr} = 0.2882$ nm [36] and the concentrations are $c_{\alpha'} = 0.95$ and $c_\alpha = 0.05$ for $c_0 = 0.2$ alloy aged at 535 K. So, the composition expansion coefficient of lattice parameter is approximately $\varepsilon_0 = (a_{Cr} - a_{Fe})/[a_{Fe}(c_{\alpha'} - c_\alpha)] = 0.006$.

The elastic constants of Fe and Cr are listed in Table 1 and Vergard's law is used to calculate the elastic constants of a Fe–Cr alloy.

3. Results and discussion

The simulations are performed with a $N \times M = 256 \times 256$ representative cell. The dimensionless time step is $\Delta t^* = 0.03$. To trigger simulations, we may add a random Gaussian distributed fluctuation in the dimensionless concentration to the representative cell at the beginning of simulations. The interval of the initial fluctuation is set to be $[-0.0025, 0.0025]$ in the present work, which is much smaller than $[-0.1, 0.1]$ used in Ref. [13]. The initial fluctuation of an infinitesimal or zero magnitude allows us to focus on the

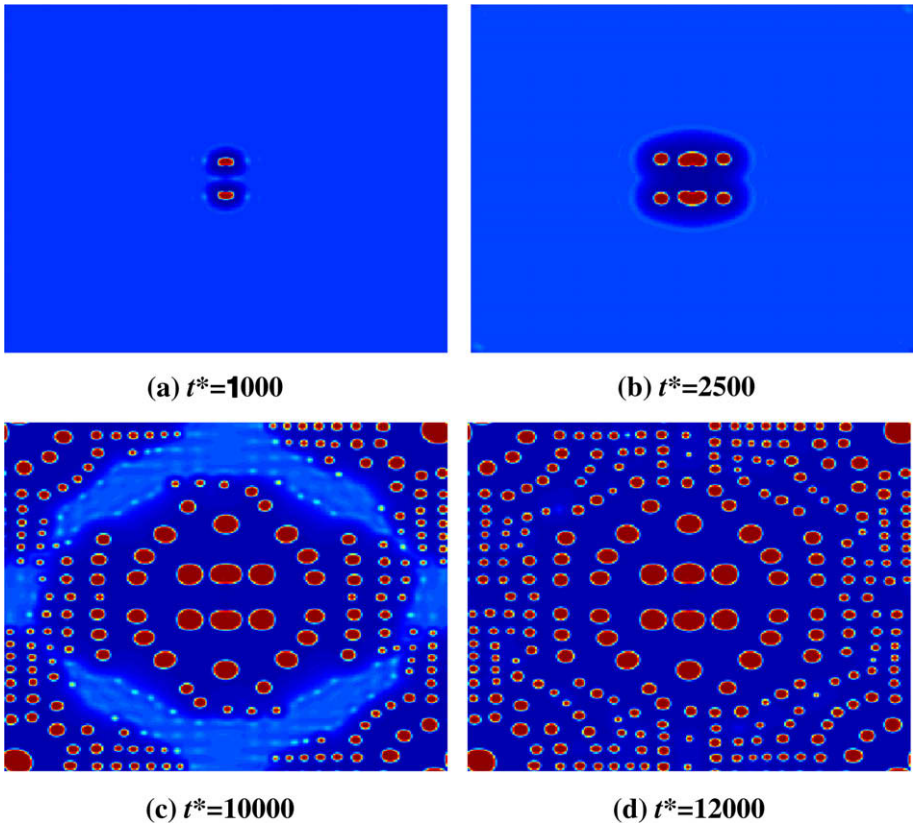

Fig. 7. Phase separation with two edge dislocations in the $c_0 = 0.2$ Fe–Cr alloy aged at 535 K without any initial fluctuation.

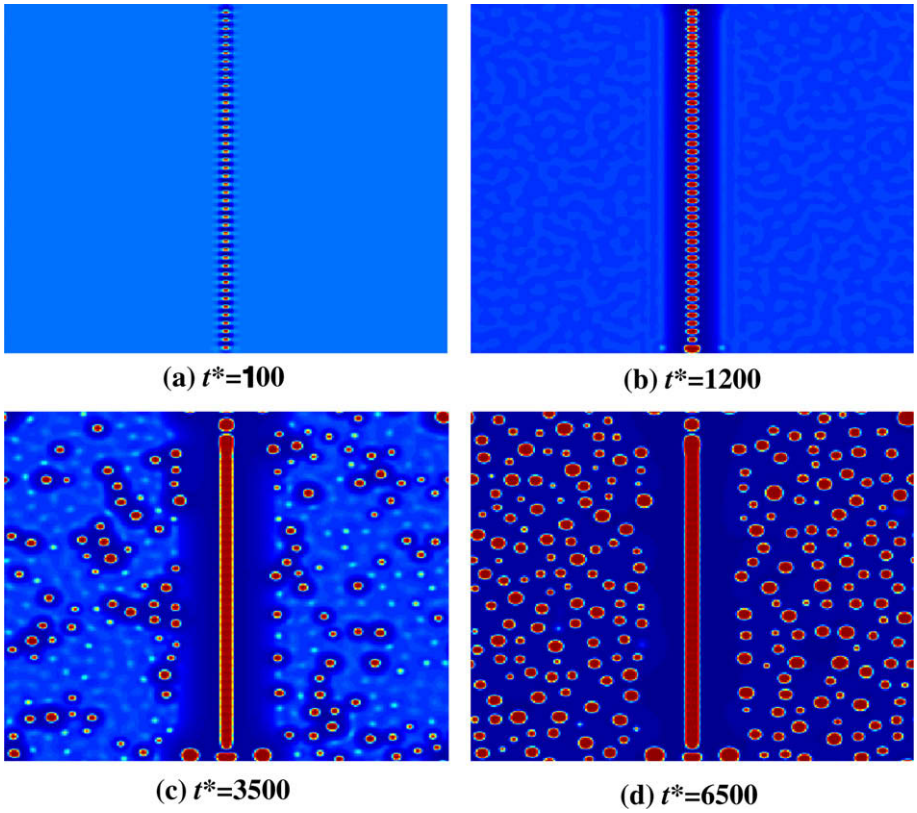

Fig. 8. Phase separation with a tilt grain boundary of $\theta = 9.55^\circ$ along line $x_1^* = 128$ in the $c_0 = 0.2$ Fe–Cr alloy aged at 535 K.

dislocation effect. Moreover, the periodic boundary condition requires that a stress component at the left boundary, σ_l, should be the same as that at the right boundary, σ_r and Eq. (18) can be only approximately calculated. In the present study, a relative error of $\delta = |(\sigma_l - \sigma_r)/\sigma_r| = 6.8\%$ was used.

3.1. Early stage of spinodal decomposition

The Fe–Cr alloy with a nominal concentration of $c_0 = 0.2$ was quenched from a homogeneous solid solution at a high temperature to temperature 535 K, as marked by point A in Fig. 1, and then aged at 535 K. Fig. 2a–f show the phase separation process of the alloy, where the red and dark blue colors illustrate Cr-enriched and Cr-depleted regions, respectively. To study the effect of dislocations on the decomposition process, two edge dislocations with Burgers' vectors of $\mathbf{b} = a_0/2[1\,1\,1]$ and $\mathbf{b} = a_0/2[\bar{1}\,\bar{1}\,\bar{1}]$ are located at coordinates (128, 118) and (128, 138) in the 256×256 representative cell, respectively. The dimensionless distance between the two dislocations is $d = 20$. The simulation exhibits that Cr atoms enrich themselves in the tensile stress regions of the two dislocations within a very short time, $t^* = 100$, and Cr-depleted regions accompanied with the Cr-enriched regions are formed simultaneously. At $t^* = 100$, the Cr-concentration in the Cr-enriched regions is still much lower than the equilibrium concentration, $c_{\alpha'} = 0.95$, of the α' phase, as shown in Fig. 3a. The two Cr-enriched clusters enrich in Cr-content and grow in size continuously. At $t^* = 400$, the Cr-content in the centers of the two Cr-enriched clusters reaches the equilibrium concentration of the α' phase, as shown in Fig. 3a, while the Cr-concentration in the Cr-depleted regions does not meet the equilibrium concentration, $c_\alpha = 0.05$, of the α phase. At $t^* = 1000$, the two Cr-depleted regions merge into a region enclosing the two Cr-enriched clusters, as shown by Fig. 2c. At $t^* = 5500$, the Cr-enriched clusters become the α' phase particles and the adjacent Cr-depleted region becomes the α phase, as shown in Fig. 3a. In the early stage of aging, phase separation occurs only at the dislocation core regions and the Cr-concentration seems to be roughly homogeneous in the rest regions even so the initial fluctuation is applied randomly to the entire representative cell. Eventually at $t^* = 4000$, Cr-enriched clusters appear in regions far away from the dislocations. In contrast, it takes only $t^* = 400$ for the Cr-enriched clusters at the dislocation cores to reach the same size of the biggest Cr-enriched cluster formed at $t^* = 4000$ in regions far away from the dislocations. Clearly, dislocations accelerate the phase separation process. As aging going on, more and more Cr-enriched clusters are formed in regions far away from the dislocations and the formed Cr-enriched clusters evolve to the α' phase, as shown in Fig. 2e. At $t^* = 5500$, the decomposition process is over and the final morphology is shown in Fig. 2f. The size of the α' phase particles around the dislocations is bigger than that in other regions. In comparison with the evolution of Cr-concentration at and near the dislocations shown in Fig. 3a, Fig. 3b illustrates the evolution of Cr-concentration of a α' phase particle, which is some distance away from the dislocations, as marked by letter F in Fig. 2f. The Cr-enriched cluster is formed at $t^* = 3800$, as shown in Fig. 3b, and its concentration profile at $t^* = 4000$ is similar to that of the Cr-enriched cluster at the dislocation cores at $t^* = 400$. The results show again that dislocations promote the decomposition process. After phase separation, there is a composition jump from the α' phase with the maximum Cr-concentration to the α phase with the minimum Cr-concentration when crossing an interface between the α'/α particles. This composition jump occurs within a narrow region ranging from $3\Delta x_1^*$ to $5\Delta x_1^*$.

As a comparison, Fig. 4 shows the phase separation process without dislocations in the same alloy aged at the same temperature with the same initial fluctuation, as those described above for Figs. 2 and 3. We may define an incubation time as the time at

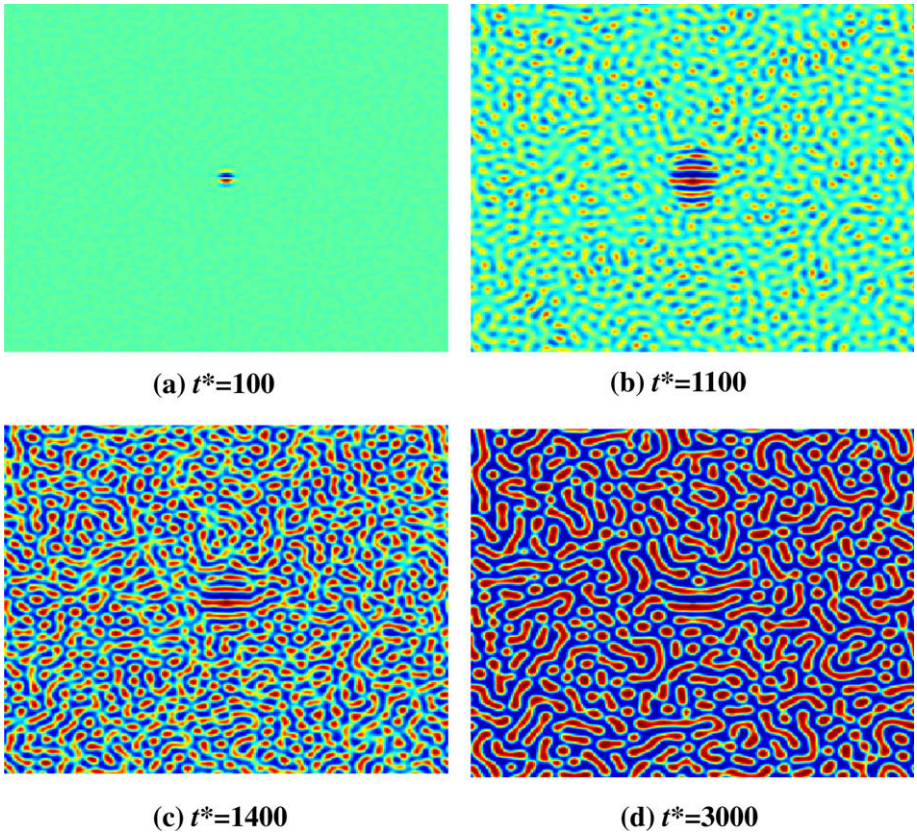

Fig. 9. Phase separation with an edge dislocation in the $c_0 = 0.45$ Fe–Cr alloy aged at 673 K.

which the equilibrium Cr-concentration of the α' phase first appears in the simulated system. Fig. 5 shows the composition evolution of the particle labeled with an arrow in Fig. 4b and c. The incubation time is about $t^* = 4000$ without dislocations, while the incubation time is about $t^* = 400$ at the dislocation cores. Comparing Fig. 3b with Fig. 5 indicates that the incubation time in regions far away from dislocations and the incubation time in the same simulated system without dislocations are almost the same, indicating that the dislocation effect on the incubation time is limited to a small region near the dislocation cores. Fig. 6 plots the nucleation time, for particles labeled with letters A, B, C, D, E and F in Fig. 2f, versus the distance from the dislocation core with coordinates (128, 118) to each particle center. Fig. 6 shows that the incubation time increases quickly to a constant value as the distance increases. The result demonstrates that the dislocation effect on the incubation time is limited to a local region near the dislocation.

In spinodal decomposition, any small composition fluctuation is able to induce the phase separation. If there are dislocations in the alloy, the dislocation stress field is inhomogeneous and may trigger the decomposition process. Thus, spinodal decomposition may be started with an initial fluctuation of an infinitesimal or zero magnitude in the simulated system, where atom migration is driven by the dislocation stress field. For example, Fig. 7 shows the simulation phase separation process of the $c_0 = 0.2$ Fe–Cr alloy aged at 535 K without any initial fluctuation. Two edge dislocations with Burgers' vectors of $a_0/2[1\,1\,1]$ and $a_0/2[\bar{1}\,\bar{1}\,\bar{1}]$ are located at coordinates (128, 118) and (128, 138), respectively. The tensile stress regions of the dislocations become Cr-enriched regions very soon, as shown in Fig. 7a, which is similar to the early stage phase separation shown in Fig. 2a–c. As aging going on, the α' phase continuously precipitates around the dislocations and the nearby regions become Cr-depleted. At $t^* = 2500$, the composition is still homogeneous and remains the nominal concentration in the regions far away from the dislocations, as shown in Fig. 7b. After aging of $t^* = 10{,}000$, the α' phase precipitates everywhere far away from the dislocations. Finally, the simulated system reaches the equilibrium state at $t^* = 12{,}000$. As mentioned above, the phase equilibrium is reached at $t^* = 5500$ if the initial fluctuation is added, as shown in Fig. 2f. The results indicate that the phase separation process with two dislocations is slower without initial fluctuation than that with the initial fluctuation. Fig. 7 shows that the α' phase particles are symmetrically distributed around the two-dislocation center, thereby implying that the symmetrical stress field of the dislocations controls the atom migration and arrangement process if no initial fluctuation is added. In this case, the final particles size near the dislocations is bigger than that in other places.

Tilt grain boundaries may play an important role in the microstructure evolution. Consider a tilt grain boundary with $\theta = 9.55°$,

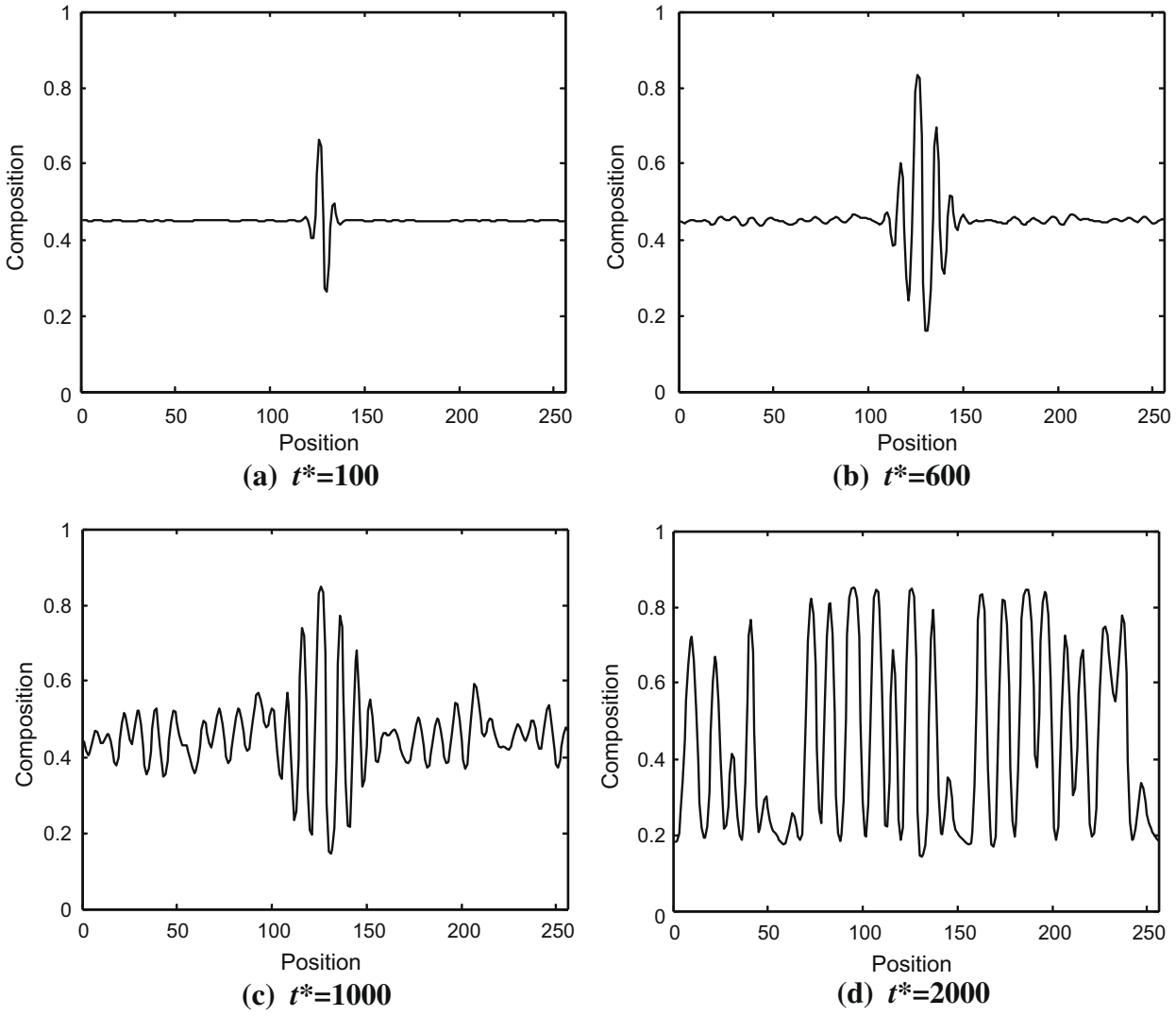

Fig. 10. Composition evolution through the dislocation center along the x_2' direction in Fig. 9.

formed by an edge dislocation wall with Burgers vector $a_0/2[1\,1\,1]$, along the line of $x_1^* = 128$ in the simulation cell, as shown in Fig. 8. The Cr-cluster is formed at the tensile stress side of the dislocations at the initial stage, as shown in Fig. 8a. Then, the Cr-depleted regions are formed at the two sides of the tilt grain boundary and the other places are still homogeneous at this time, as shown in Fig. 8b. At $t^* = 3500$, some of the α' phase particles have precipitated in regions far from the tilt grain boundary. When the system reaches the equilibrium state, there is a band region of α' phase along the tilt grain boundary, and Cr-depleted regions beside the band. The morphology in regions far away from the tilt boundary looks normal.

3.2. Final spinodal decomposition pattern

As mentioned above, dislocations enhance greatly the phase separation process. Particularly at the early stage of aging, the phase separation occurs only at and near dislocations. In this part, we study the dislocation effect on the modulated structure of a $c_0 = 0.45$ Fe–Cr alloy aged at 673 K (point B in Fig. 1). Fig. 9 shows the spinodal decomposition process with an edge dislocations of Burgers' vector of $a_0/2[1\,1\,1]$ located at coordinates (128, 128) and a random initial fluctuation with the interval [−0.0025, 0.0025], which are the same as that used before for Figs. 2 and 3. At the initial stage, Cr atoms enrich and deplete themselves at the dislocation core regions and reach the equilibrium concentration of $c_{\alpha'} = 0.88$ at $t^* = 600$, as shown in Figs. 9a, b and 10b. This stage is similar to that of the $c_0 = 0.2$ alloy aged at 535 K with two dislocations shown in Fig. 2a–c. However, the velocity of spinodal decomposition in regions far away from the dislocations is faster than that in the $c_0 = 0.2$ alloy aged at 535 K. In the regions far away from the dislocations, as shown in Fig. 10c, the obvious composition inhomogeneity occurs at $t^* = 1000$ and the composition reaches the equilibrium at $t^* = 2000$ in the $c_0 = 0.45$ alloy aged at 673 K, whereas the two corresponding times are $t^* = 3800$ and $t^* = 4000$ for the earlier precipitated particles in the $c_0 = 0.2$ alloy aged at 535 K, as shown in Fig. 3b. The entire spinodal morphology with a dislocations is featured by a dislocation modified modulated structure, as shown in Fig. 9, meaning that the morphology near the dislocations is determined by the dislocation stress field.

Fig. 11 shows the effect of a tilt grain boundary with $\theta = 9.55°$ along the line of $x_1^* = 128$ in the simulation cell for the $c_0 = 0.45$ alloy aged at 673 K. Comparing Fig. 11a with Fig. 8a indicates that the initial composition variation in the $c_0 = 0.45$ alloy is similar to that in the $c_0 = 0.2$ alloy. At time $t^* = 1100$, obvious composition fluctuation occurs in regions far away from the tilt grain boundary. At $t^* = 1400$, the Cr-depleted regions are formed beside the tilt grain boundary and α' phase precipitates at the regions far away from the tilt grain boundary. When the system reaches the equilibrium state, as shown in Fig. 11d, the α' phase has an unconnected band shape beside the two Cr-depleted regions, while the regular modulated spinodal morphology appears in the regions far away from the tilt grain boundary. This is because the tilt grain boundary can accommodate a finite amount of Cr atoms and leads to a local change in composition along the tilt grain boundary.

Fig. 12a–c shows the morphologies of the $c_0 = 0.45$ alloy aged at 673 K with a tilt grain boundary of tilt angles $\theta = 1.91°$, 5.73° and 9.55°, respectively. When the tilt angle of grain boundary is small, 1.91° or 5.73°, the Cr atoms enrich themselves in the tensile stress side of the dislocations and form the horizontal orientation block shape α' phase in the tilt grain boundary region, as shown in Fig. 12a and b. When the tilt angle is 9.55°, however, the continuous α' phase is formed along the tilt grain boundary with two Cr-depleted regions beside. This is because when the tilt angle is larger, the dislocation spacing is shorter and α' phase participates will be accommodated by the dislocations. To investigate further the effect of tilt grain boundaries on the decomposition morphology, we simulate spinodal decomposition in the $c_0 = 0.45$ alloy aged at

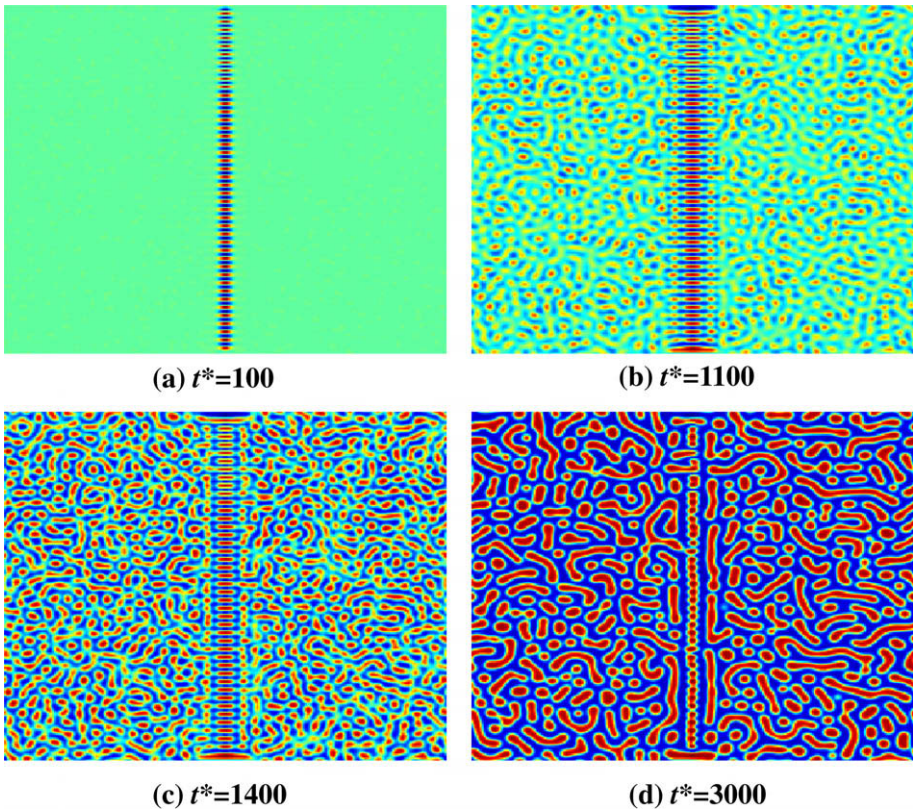

Fig. 11. Phase separation with a tilt grain boundary of $\theta = 9.55°$ along line $x_1^* = 128$ in the $c_0 = 0.45$ Fe–Cr alloy aged at 673 K.

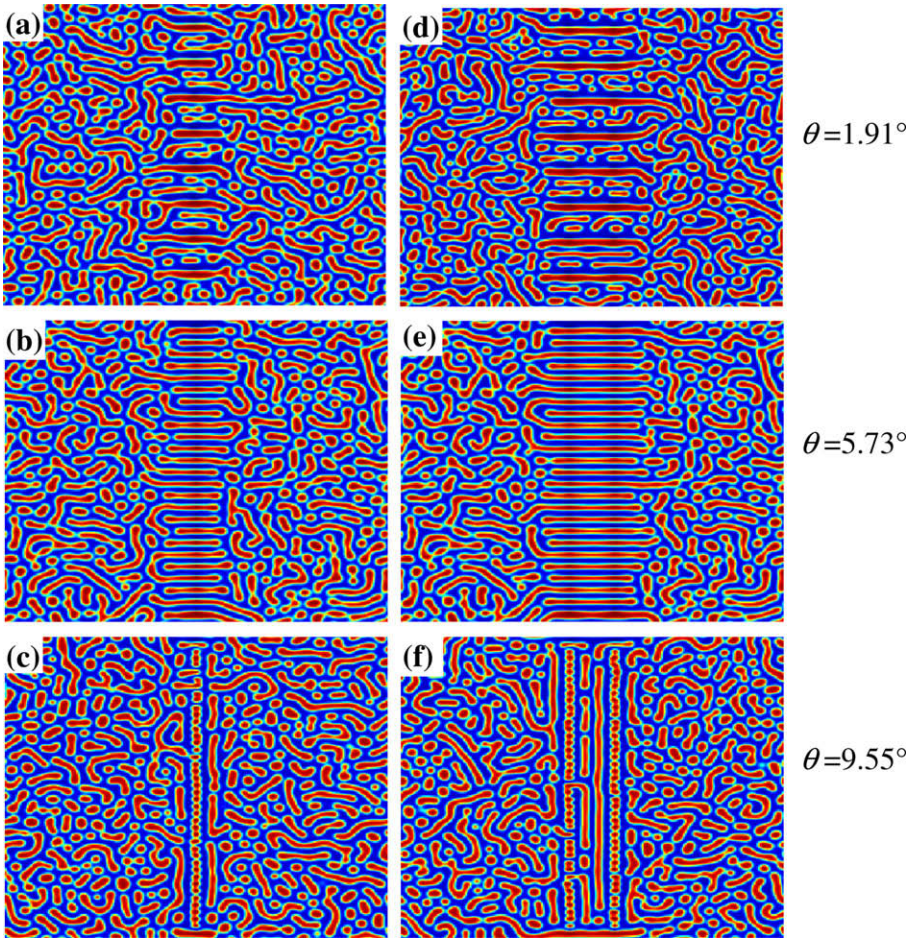

Fig. 12. Phase separation with a tilt grain boundary along line $x_1^* = 128$ in (a)–(c), and with two tilt grain boundaries along lines $x_1^* = 113$ and $x_1^* = 143$ in (d)–(f) of different tilt angles in the $c_0 = 0.45$ Fe–Cr alloy aged at 673 K for $t^* = 3000$.

673 K with two tilt grain boundaries along lines of $x_1^* = 113$ and $x_1^* = 143$, respectively. Fig. 12d–f shows the decomposition morphology for the tilt angles of $\theta = 1.91°$, 5.73° and 9.55°, respectively. As expected, the decomposition morphology with two tilt grain boundaries is correspondingly similar to that with one tilt grain boundary, except that the horizontal orientation block shape for $\theta = 1.91°$ and 5.73° becomes big and there are two columns of α' phase for $\theta = 9.55°$ due to the two column tilt angle boundaries.

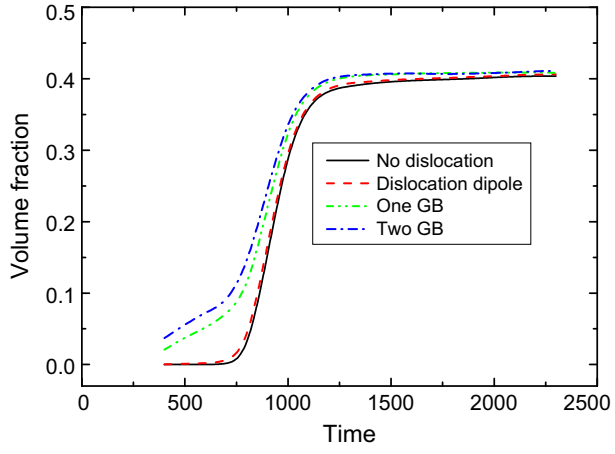

Fig. 13. Volume fraction of precipitates as a function of aging time for the $c_0 = 0.45$ Fe–Cr alloy aged at 673 K, where one and two column tilt grain boundaries (GB) are all with a tilt angle $\theta = 5.73°$.

Since dislocations make the phase decomposition faster, the effect of tilt grain boundaries on the velocity of phase decomposition is shown by plotting the volume fraction of α' phase as a function of aging time, as shown in Fig. 13 for the $c_0 = 0.45$ alloy aged at 673 K. Since the volume fraction of α' phase eventually reaches its equilibrium value, the effect is significant at the initial stage of phase decomposition. Before the time $t^* = 1000$, the volume fraction increase quickly with one and two tilt grain boundary than that without or with only one dislocation and, as expected, the volume fraction with two tilt grain boundaries is larger than that of with one tilt grain boundary. One dislocation has little influence on the volume fraction because its influence is very much localized at the dislocation core region.

4. Concluding remarks

The effect of dislocations and tilt grain boundary on the spinodal decomposition of Fe–Cr alloy was simulated by using the phase-field method. The simulation results illustrate that the dislocation stress field makes the phase separation faster near the area of dislocations. At the equilibrium state, the size of the α' phases at the dislocation is bigger than the place far away from the dislocations for the low concentration alloys. The tilt grain boundary produces different orientation morphologies as the tilt angle changes. Even without any initial fluctuation in composition, a dislocation stress field is able to trigger the phase separation process. It is generally

believed that thermal fluctuation occurs at a finite temperature and the thermal fluctuation is expressed in terms of Langevin force in phase-field simulations [39]. In practice, the defined Langevin force is usually so high such that a reduction factor is generally applied [40]. The magnitude of a used thermal fluctuation or a used initial fluctuation changes simulation results if the magnitude is too high [40]. To focus on the dislocation effect, we do it on purpose in the present phase-field simulations by using an initial fluctuation with a low magnitude or without using any initial fluctuation.

Acknowledgments

The authors would like to acknowledge the support by Nansha Science & Technology Bureau (NSTB) (JRC-08-GD-002A) and HK-BJ UST JRC's operating budget (JRC-08-GD-002B).

References

[1] J.W. Cahn, Acta Metall. 5 (1957) 169.
[2] C.C. Dollins, Acta Metall. 18 (1970) 1209.
[3] A.H. Cottrell, B. Bilby, Proc. Phys. Soc. (London) A 62 (1949) 49.
[4] F.S. Ham, J. Appl. Phys. 30 (1959) 915.
[5] S. Harper, Phys. Rev. 83 (1951) 709.
[6] I. Singer-Loginova, H.M. Singer, Prog. Phys. 71 (2008) 106501.
[7] L.Q. Chen, Annu. Rev. Mater. Res. 32 (2002) 113.
[8] X.H. Guo, S.Q. Shi, Q.M. Zhang, X.Q. Ma, J. Nucl. Mater. 378 (2008) 110.
[9] S.Y. Hu, C.H. Henager Jr., H.L. Heinisch, M. Stan, M.I. Baskes, S.M. Valone, J. Nucl. Mater. 392 (2009) 292.
[10] S. Sreekala, M. Haataja, Phys. Rev. B 76 (2007) 094109.
[11] J.W. Cahn, Acta Metall. 9 (1961) 795.
[12] J.W. Cahn, J.E. Hilliard, J. Chem. Phys. 42 (1965) 93.
[13] F. Léonard, R.C. Desai, Phys. Rev. B 58 (1998) 8277.
[14] Y. Ni, L.H. He, Thin Solid Films 440 (2003) 285.
[15] S.Y. Hu, L.Q. Chen, Acta Mater. 52 (2004) 3069.
[16] A. Minami, A. Onuki, Phys. Rev. B 70 (2004) 184114.
[17] C. Shen, N. Zhou, Y.Z. Wang, Metall. Mater. Trans. A 39 (2008) 1630.
[18] Y.U. Wang, Y.M. Jin, A.M. Cuitiño, A.G. Khachaturyan, Phil. Mag. Lett. 81 (2001) 385.
[19] S.Y. Hu, J. Choi, Y.L. Li, L.Q. Chen, J. Apply. Phys. 96 (2004) 229.
[20] S.Y. Hu, L.Q. Chen, Acta Mater. 49 (2001) 463.
[21] T. Mura, Micromechanics of Defects in Solids, Kluwer Academic Publisher, Dordrecht, 1982.
[22] V.K. Shamardin, V.N. Golovanov, T.M. Bulanova, A.V. Povstianko, A.E. Fedoseev, Yu.D. Goncharenko, Z.E. Ostrovsky, J. Nucl. Mater. 271–272 (1999) 155.
[23] E. Lucon, R. Chaouadi, M. Decreton, J. Nucl. Mater. 329–333 (2004) 1078.
[24] K. Shiba, M. Suzuki, A. Hishinuma, J. Nucl. Mater. 237 (1996) 309.
[25] F. Danoix, P. Auger, Mater. Charact. 44 (2000) 177.
[26] R.L. Klueh, K. Ehrlich, F. Abe, J. Nucl. Mater. 191–194 (1992) 116.
[27] M.K. Miller, K.F. Russel, Surf. Sci. 266 (1992) 232.
[28] M.K. Miller, J.M. Hyde, M.G. Hetherington, A. Cerezo, G.D.W. Smith, C.M. Elliott, Acta Metall. Mater. 43 (1995) 3385.
[29] J.M. Hyde, M.K. Miller, M.G. Hetherington, A. Cerezo, G.D.W. Smith, C.M. Elliott, Acta Metall. Mater. 43 (1995) 3403.
[30] J.M. Hyde, M.K. Miller, M.G. Hetherington, A. Cerezo, G.D.W. Smith, C.M. Elliott, Acta Metall. Mater. 43 (1995) 3415.
[31] J.O. Andersson, B. Sundman, Calphad 11 (1987) 83.
[32] J.E. Hilliard, Phase Transformations, ASM International, Metal Park, OH, USA, 1970.
[33] M. Honjo, Y. Saito, ISIJ Int. 40 (2000) 914.
[34] A.G. Khachaturyan, Theory of Structure Transformation in Solids, John-Wiley and Sons, New York, 1983.
[35] T.C.T. Ting, Anisotropy Elasticity, Theory and Applications, Oxford Science Publications, New York, 1996.
[36] T.Y. Zhang, J. Appl. Phys. 78 (1995) 4948.
[37] T.Y. Zhang, Defect Diffus. Forum 136–137 (1996) 61.
[38] E.A. Brandes, G.B. Brook, Smithells Metals Reference Book, seventh ed., Butterworth-Heinemann, Oxford, 1997.
[39] C. Shen, J.P. Simmons, Y. Wang, Acta Mater. 55 (2007) 1457.
[40] R. Poudri, L.Q. Chen, Acta Mater. 46 (1998) 3915.